Multi-physics optimization of three-dimensional microvascular polymeric components

Alejandro M. Aragón [a,*], Rajat Saksena [c], Brian D. Kozola [b], Philippe H. Geubelle [b], Kenneth T. Christensen [b,c], Scott R. White [b]

[a] Civil and Environmental Engineering Department, University of Illinois, 205 North Mathews Avenue, Urbana, IL 61801, USA
[b] Aerospace Engineering Department, University of Illinois, 104 South Wright Street, Urbana, IL 61801, USA
[c] Department of Mechanical Science and Engineering, University of Illinois, 1206 W. Green St., Urbana, IL 61801, USA

A R T I C L E   I N F O

A B S T R A C T

This work discusses the computational design of microvascular polymeric materials, which aim at mimicking the behavior found in some living organisms that contain a vascular system. The optimization of the topology of the embedded three-dimensional microvascular network is carried out by coupling a multi-objective constrained genetic algorithm with a finite-element based physics solver, the latter validated through experiments. The optimization is carried out on multiple conflicting objective functions, namely the void volume fraction left by the network, the energy required to drive the fluid through the network and the maximum temperature when the material is subjected to thermal loads. The methodology presented in this work results in a viable alternative for the multi-physics optimization of these materials for active-cooling applications.

1. Introduction

By mimicking circulatory systems found in many living organisms, microvascular materials have been the focus of renewed interest recently for their potential in providing a wide range of added functionality to polymers and polymeric matrix composites (PMC). Some of these multi-functionalities include active cooling [1,2], and autonomic healing [3,4]. Beyond the need to use materials more efficiently, this renewed interest in multifunctional microvascular materials can also be attributed to recent advances in manufacturing techniques. Traditionally, the writing process of the microvascular network is in 2D, and 3D scaffolds by superimposing 2D layers [5]. However, new methodologies are being explored such as the omnidirectional printing (ODP) technique, where a 3D structure is extruded within a gel that serves as a support [6]. Another approach proposed recently in the creation of fiber-reinforced composites uses sacrificial fibers to create the embedded network by depolymerization and volatilization [7]. These techniques allow for the creation of complex 3D embedded networks of microchannels in polymeric and PMC components.

This paper focuses on the design of microvascular materials for active cooling applications. The computational design of this class of materials is an intricate process, due to the large number of design variables (e.g., network topology, channel diameters) and the multiple competing objective functions that define the design process. The computational design tool to be developed must be capable of capturing the trade-offs between these competing objectives. For example, microvascular

* Corresponding author. Present address: EPFL ENAC IIC LSMS, Laboratoire de Simulation en Mécanique des Solides, Bât. GC A2 505, Station 18, CH-1015 Lausanne, Switzerland. Tel.: +41 21 693 24 18; fax: +41 21 693 63 40.
  E-mail addresses: alejandro.aragon@fulbrightmail.org (A.M. Aragón), rsaksen2@illinois.edu (R. Saksena), brian.kozola@navy.mil (B.D. Kozola), geubelle@illinois.edu (P.H. Geubelle), ktc@illinois.edu (K.T. Christensen), swhite@illinois.edu (S.R. White).

networks designed for flow efficiency are likely to have a topology that is very different from those designed for structural integrity or thermal control. Because of the computationally intensive nature of the optimization methodology, we are not only interested in the optimized network topologies, but also in obtaining an efficient and accurate evaluation of the objective functions and constraints involved in the optimization. Several approaches can be used to design the microvascular networks embedded in these materials. These include (i) semi-analytical approaches; (ii) gradient-based search methods; and (iii) evolutionary algorithms. Semi-analytical approaches can be used to solve network optimization problems that do not involve a large set of optimization variables. These methods often require *a priori* information about the optimal solution. Constructal theory [8,9] lies in this group, and it has been used for the solution of simple problems [10–12]. Within gradient-based search techniques, topology optimization has been used recently to optimize flow networks [13]. This method involves design variables that are continuous and often leads to an optimal solution that is local, so finding a global optimal solution is not guaranteed. Evolutionary algorithms (EAs) comprise the last category by borrowing some concepts from biological evolution. As a subset of this group, genetic algorithms (GAs) [14,15] are population-based algorithms that improve a set of candidate solutions throughout their evolution, by applying genetic operators *selection*, *crossover* and *mutation*. The survival of the fittest takes place through selection, preventing the worst candidates to be nominated for reproduction. The distinction among individuals is conducted through the computation of one or more objective functions, which quantitatively describe how fit the individuals are to solve the problem. Through the crossover operator, new candidate solutions are created by mixing the information of those nominated through the selection process. The mutation operator modifies slightly the features of an individual and could introduce new features to the existing solutions. GAs offer several advantages compared to the other two aforementioned methods. GAs can use discrete or continuous variables, and they search the entire decision space, so optimal solutions found are likely to be global optima. Furthermore, there is no need for *a priori* knowledge about optimal solutions, but this information can be used to obtain a starting population with those features in the so-called knowledge-based GAs.

The simple genetic algorithm (SGA) [14] is one of the most common algorithms in this group and is used with a single objective function, usually determined as a linear combination of weighted objectives if the optimization is on several objectives. In multi-objective genetic algorithms (MOGAs) [16], individuals are compared in all objective functions using a Pareto-optimality procedure. In this context, an individual is better than another if it is better in at least one objective function and it is not worse in the rest. This selection mechanism, which has been borrowed from the field of economics, leads to a powerful method for obtaining an optimal front (called Pareto-optimal), where all individuals lying on it are optimal solutions to the multi-objective optimization problem. By supplementing the MOGA with a mechanism that deals with constraints, a powerful methodology for multiple-objective constrained optimization is obtained. This is the method chosen in our work because it allows us to visualize the trade-offs between conflicting objective functions. The GA-based optimization tool can be used to study multi-physics optimization problems for which the objective functions involved describe different physical phenomena. In the context of active cooling applications, the temperature field is obtained when the polymeric component is subjected to thermal loads. To obtain the temperature distribution in the microvascular material, one needs to solve for the temperature field in both the solid and fluid domains. This problem is referred to in the literature as the conjugate heat transfer problem. However, this approach is not straightforward because of the coupling that exists between fluid and solid domains if a non-monolitic solution approach is used. This means that an iterative approach is needed to obtain a converged value of the temperature at solid–fluid boundaries. Because the MOGA typically requires thousands of objective function evaluations, and the total CPU time is directly proportional to the cost of these objective functions, we resort to a simplified formulation that describes the convective heat transfer in the microchannels by collapsing them to line heat sinks (or heat sources) over linear segments and solving for the heat equation only in the solid. Therefore, the temperature distribution in the solid domain will have a discontinuous gradient across the microchannels.

The multi-physics optimization of microvascular materials for 2D problems in the context of active-cooling applications has been presented by Aragón et al. [2], who coupled the multi-objective constrained optimization framework described in [17] with a physics solver based on a generalized finite element method described in [18]. The application of the resulting multi-physics optimization tool to several thermal problems demonstrated the existence of well-defined Pareto-optimal fronts for objective functions related to the void volume fraction and flow efficiency of the embedded network, its impact on the maximum temperature predicted in the microvascular component, and the associated surface convected energy. This paper extends the methodology presented in [2] to fully 3D networks, motivated by recent advances in the manufacturing processes, which allow for the creation of complex 3D network topologies [6,7], and by the desire to eliminate some of the assumptions behind the 2D thermal models of the microvascular actively cooled component [2].

This paper is organized as follows: Section 2 states the optimization problem and presents the mathematical model used for representing the microvascular material. Section 3 presents a brief overview of GA optimization scheme. The objective functions and constraints used in conjunction with the GA are defined in Section 4, followed in Section 5 by a validation study of the thermal field when these materials are used for active cooling applications. Finally, the application of the optimization framework for the design of 3D microvascular networks follows in Section 6.

2. Microvascular network representation

Consider the mathematical model of a biomimetic material shown in Fig. 1. An open domain $\Omega \subset \mathbb{R}^3$, with boundary $\Gamma := \overline{\Omega} - \Omega$, represents the polymeric component. The optimization process starts from a microvascular *network template*
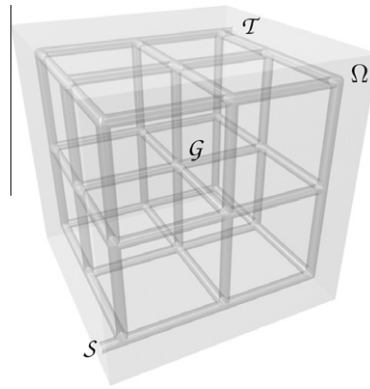
Fig. 1. Mathematical model of a biomimetic polymeric component. A domain Ω embeds a microvascular network represented by a graph $\mathcal{G}$. Inflow and outflow vertex sets $\mathcal{S}$ and $\mathcal{T}$, respectively, are also shown in the figure.

[17,2], a reference structure that contains every possible microchannel considered in the design. Mathematically, the network template is represented by a graph $\mathcal{G} := (\mathcal{V}, \mathcal{E})$, where each edge $e \in \mathcal{E}$ represents a channel of the network and each vertex $v \in \mathcal{V}$ represents the possible location of a microchannel endpoint. Thus, a spatial coordinate $\mathbf{x}_v \subset \Lambda \subset \overline{\Omega}$ is associated with each vertex v, where $\Lambda := \left\{ \sum_{i=1} z_i \mathbf{e}_i \mid z_i \in \mathbb{Z} \right\}$ is a three-dimensional point lattice and $\mathbf{e}_i$ represents the ith component of an orthogonal basis of $\mathbb{R}^3$. Restricting the location of the vertices to a point lattice reduces considerably the number of possible network topologies within the polymeric component. Other properties assigned to vertices include pressure $p_v : v(\mathcal{V}) \to \mathbb{R}$ and mass flow rate $\dot{m}_v : v(\mathcal{S} \cup \mathcal{T}) \to \mathbb{R}, \mathcal{S} \cap \mathcal{T} = \emptyset$, where $\mathcal{S}$ and $\mathcal{T}$ represent inflow and outflow vertex sets, i.e., $\{\mathcal{S}, \mathcal{T}\} \subseteq \mathcal{V}(\mathcal{G})$. Because of mass conservation, the total mass inflow rate $\dot{m}_\mathcal{S} := \sum_{v \in \mathcal{S}} \dot{m}_v$ equals the total mass outflow rate $\dot{m}_\mathcal{T} := \sum_{v \in \mathcal{T}} \dot{m}_v$. Properties are also assigned to the edges of the graph, including the microchannel diameter $D_e : e(\mathcal{E}) \to \mathbb{R}$, length $L_e : e(\mathcal{E}) \to \mathbb{R}$, and mass flow rate $\dot{m}_e : e(\mathcal{E}) \to \mathbb{R}$.

These microvascular materials are often created by extruding a fugitive ink on a polymeric substrate. Let $\mathcal{D} = \{D_i\}_{i=1}^k$ be the set of discrete diameters used in the optimization process. This set includes the diameters prescribed by the manufacturing process, i.e., the diameter of the nozzles used to extrude the fugitive ink. It also includes $D_k = 0$, which represents the absence of a microchannel to allow networks to change in topology from that of the network template. During the optimization process, each microchannel $e \in \mathcal{E}$ of a candidate solution is assigned a diameter $D_e \in \mathcal{D}$ in order to optimize a set of objective functions $\Phi = \{\phi_i\}_{i=1}^m$, subject to a set of constraints $\Psi = \{\psi_i\}_{i=1}^n$. Each candidate solution created during the GA optimization process can be thought of as a mapping, a function $f : \mathcal{G} \to \mathcal{G}' \subseteq \mathcal{G}$, where $\mathcal{G}' := (\mathcal{V}', \mathcal{E}')$ may contain fewer channels, i.e., $\mathcal{E}' \subseteq \mathcal{E}$. Thus, the *degree* of a vertex v' in the candidate solution, denoted $\deg(v')$ and defined as the number of incident edges on the vertex, may be smaller than the degree of the corresponding vertex in the network template $\mathcal{G}$, i.e., $\deg(v' \in \mathcal{V}') \leqslant \deg(v \in \mathcal{V})$. It is interesting to note that there are $k^{|\mathcal{E}|}$ possible network configurations in this optimization process. Yet many of these topologies are considered unfeasible because there is no solution for the flow problem, as explained in the Section 4. In other words, their corresponding graphs are *disconnected*, which means that there is at least one pair of vertices $v_i', v_j' \in \mathcal{V}'(\mathcal{G}')$ for which a path cannot be created through the existing edges $\mathcal{E}'(\mathcal{G}')$. A disconnected graph therefore contains two or more *connected components*.

3. Multi-objective constrained genetic algorithms

Genetic algorithms are chosen as the underlying optimization technique because of their advantages with regard to other methods used in search and optimization. As a subset of a broader category of evolutionary algorithms (EAs), genetic algorithms are population-based methods where candidate solutions develop towards better configurations for the problem considered throughout an evolution process. GAs do not require any information about optimal topologies, a main advantage when comparing the method with other approaches used for optimization such as constructal theory [8,10,19]. Usually, the starting population of a GA is created randomly, yet any *a priori* knowledge about optimal features can be incorporated into this initial population, procedure known as a knowledge-based GA. After the creation of the initial population, GAs usually start the evolution over a specified number of generations $t_{\max}$, unless other criterion is used to obtain a measure of convergence. More precisely, GAs can evolve indefinitely introducing new features to individuals in the population. GAs do not guarantee the convergence to optimal solutions at any value of $t_{\max}$, but they search the entire decision space, a main advantage when comparing GAs to gradient-based search techniques like topology optimization [20,21,13]. Also, GAs do not require any gradient computation, and they can be used as long as a quantitative measure of the fitness can be assigned to the individuals in the population. Additionally, GAs can handle problems that are encoded with both discrete and continuous variables. As explained in Section 2, the optimization problem in this work assigns discrete values to the diameters of the microchannels of candidate solutions, making this a discrete optimization problem.

At each generation t of the evolution of the GA, the genetic operators *selection*, *crossover* and *mutation* are applied to generate the population at generation $t + 1$. The selection operator can be thought of as a mechanism that eliminates those individuals with low fitness so that they are excluded in successive generations, thus fulfilling Darwin's natural selection. Through the crossover operator, selected individuals exchange their features to produce new individuals. As a result, the created individuals contain features found in their parents. Finally, the mutation operator slightly modifies the characteristics of the newly created individuals and can bring new features not present in their parents nor in the entire population. In this work, tournament selection, uniform crossover and bitwise mutation are used as genetic operators [14,15]. It is worth noting that bitwise mutation can only be applied if $k = 2$. If more diameters are considered, Gaussian mutation can be used as the mutation operator [17]. The simple GA [14] employs only the genetic operators mentioned above to determine the population at generation $t + 1$. However, when dealing with multiple objective functions, it is better to use a Pareto selection mechanism to determine the population at generation $t + 1$. Through this procedure, individuals are compared in all objective functions simultaneously, and *dominated* candidates are likely to be discarded in subsequent generations. When comparing two contenders, the dominated individual is worse in at least one objective function while not being better in the rest. The concept of dominance is due to Pareto [22] from the field of economics.

Having the genetic operators for the creation of new candidate solutions and the Pareto selection mechanism to deal with multiple objectives, the remaining challenge involves the consideration of constraints. The explanation given in the previous paragraph deals with the objective function space. Similarly, we can apply the same ideas to a space dealing with constraints, thus better individuals can be thought of being "less unfeasible". However, this approach works only when dealing with unfeasible individuals. If at a particular generation t, the population is composed of both feasible and unfeasible candidates, the strategy adopted in this work to determine the better of two contenders is as follows: If one individual is feasible and the other is not, the feasible individual is selected. If both individuals are unfeasible, select the less unfeasible one based on the values of the constraints. Finally, if both individuals are feasible or if an individual cannot be selected because they have the same constraint values, select the best individual in the objective function space. In this work, the nondominated sorting genetic algorithm II (NSGA-II) [23] with the addition of a constraint space is used as the multi-objective constrained genetic algorithm. For more information, refer to [17,2].

The evolution of a GA requires a large number of evaluations, thus obtaining meaningful results can be computationally demanding. However, the evaluation part of the GA is *embarrassingly parallel*, which means that candidate solutions can be evaluated in different processes independently. This property of the GAs make them suitable for distributed-memory machines. The algorithm used in this work adopts a master–slave approach, where the master process sends the individuals so that they can be evaluated independently by the slave processes, and then the master process collects the results afterwards. Close to ideal speed-ups are obtained using this approach. A description of the parallelization scheme adopted in this work is given in [2].

4. Design objectives and constraints

This section describes the objective functions and constraints taken into account in the 3D microvascular network design problem.

4.1. Void volume fraction

The void left by the microvascular network has a direct impact in the mechanical properties of the resulting polymer. It is desired to keep the void volume fraction to a minimum in order to reduce the network's impact on the stiffness and strength of the material. The void volume fraction objective function is defined as a function $\phi_v : \mathcal{E}'(\mathcal{G}') \to \mathbb{R}$:

$$\phi_v := \pi \frac{\sum_{e' \in \mathcal{E}'} L_{e'} D_{e'}^2}{4V_\Omega}, \tag{1}$$

where, in other words, the volume of the network is normalized by the volume of the polymeric component V_Ω.

4.2. Flow efficiency

Flow efficient networks will have a configuration such that the energy needed to drive the fluid through the microchannels is kept to a minimum. The quantitative evaluation of the flow efficiency is carried out through the computation of the maximum pressure drop in the network. Assuming laminar flow, a reasonable conjecture for the range of applications of these materials [24], the pressure drop in microchannel $e' \in \mathcal{E}'$ can be expressed through the Hagen–Poiseuille's law:

$$\Delta p_{e'} = \frac{128 v L_{e'}}{\pi D_{e'}^4} \dot{m}_{e'}, \tag{2}$$

where v is the kinematic viscosity of the fluid. Using Eq. (2) to express the mass flow rate at microchannel endpoints gives a total of $2|\mathcal{E}'|$ equations, which are used to assemble the system of linear equations $\vec{K}\vec{p} = \vec{m}$. In this system, $\vec{K}$ is the network characteristic matrix, $\vec{p}$ is the network pressure vector and $\vec{m}$ is the network mass flow rate vector [25,17]. This system is

solved after applying flow boundary conditions, which include prescribed mass flow rate at inflow vertices $v' \in \mathcal{S}$ and pre-scribed pressure at outflow vertices $v' \in \mathcal{T}$. Then the flow efficiency objective function is defined as a function $\phi_f : \mathcal{V}(\mathcal{G}') \to \mathbb{R}$ such that

$$\phi_f := \max_{v'_i, v'_j \in \mathcal{V}'} | p_{v'_i} - p_{v'_j} | . \tag{3}$$

More precisely, the computation of the maximum pressure drop is performed in each connected component of the graph $\mathcal{G}'$, each one with its own flow boundary conditions. That is, it is possible that during the mapping process that creates a new candidate solution, a disconnected network with two or more connected components is created. As long as those connected components have valid boundary conditions for the flow problem, the networks are considered as feasible and the computation of the maximum pressure drop is carried out component by component.

4.3. Thermal field

By obtaining the temperature field in the polymer, objective functions can be defined to obtain highly efficient networks for active cooling applications. Consider the boundary of the domain Γ with outward normal $\mathbf{n}$, partitioned in regions Γ_u, Γ_q, and Γ_h, which correspond to regions with applied Dirichlet, Neumann, and Robin boundary conditions, respectively. These regions are mutually exclusive, thus $\Gamma_u \cap \Gamma_q \cap \Gamma_h = \emptyset$. Also, the closure of their union defines the entire boundary of the poly-meric compound, i.e., $\Gamma = \overline{\Gamma_u \cup \Gamma_q \cup \Gamma_h}$. It can be shown through an energy balance [26] that the heat rate per unit length q_e in the wall of microchannel e is given by

$$q_e = \dot{m}_e c_p \frac{du}{d\xi_e}, \tag{4}$$

where u denotes temperature, c_p the specific heat of the fluid, and ξ_e the local axial coordinate of the channel. By adopting Eq. (4), several simplifying assumptions have been made, including a fully developed temperature profile and a constant heat rate along the wall of the channel. Network microchannels can be collapsed to 1D line segments due to their high aspect ratios and the small diameters used. Thus, Eq. (4) allows us to consider the cooling effect of the microchannels as heat sinks over their collapsed lines. The steady-state thermal boundary value problem is given as follows: Given fluid density ρ and fluid specific heat c_p constants, ambient temperature u_∞, the thermal conductivity tensor $\boldsymbol{\kappa} : \overline{\Omega} \to \mathbb{R}^3 \times \mathbb{R}^3$, the heat source $f : \Omega \to \mathbb{R}$, heat transfer coefficient $h : \Gamma_h \to \mathbb{R}$, and prescribed heat flux $\bar{q} : \Gamma_q \to \mathbb{R}$, find the temperature field $u : \overline{\Omega} \to \mathbb{R}$ such that

$$\nabla \cdot (\boldsymbol{\kappa}\nabla u) + f = \delta(\mathbf{x} - \mathbf{x}_e) c_p \dot{\mathbf{m}}_e \cdot \nabla u \quad \text{on } \Omega, \tag{5}$$

with $\dot{\mathbf{m}}_e = \dot{m}_e \mathbf{e}_{\xi_e}$, and boundary conditions

$$u = \bar{u} \quad \text{on } \Gamma_u, \tag{6}$$
$$\boldsymbol{\kappa}\nabla u \cdot \mathbf{n} = \bar{q} \quad \text{on } \Gamma_q, \tag{7}$$
$$\boldsymbol{\kappa}\nabla u \cdot \mathbf{n} = h(u_\infty - u) \quad \text{on } \Gamma_h. \tag{8}$$

In Eq. (5), the term on the right hand side implies summation over all network microchannels and the Dirac delta function allows us to represent the 1D microchannels within the 3D computational domain.

For the weak formulation, let $\mathcal{U} = \{u \mid u|_{\Gamma^u} = \bar{u}\} \subset H^1(\overline{\Omega})$ be the set of trial solutions for the temperature field and $\mathcal{V} = \{v \mid v|_{\Gamma^u} = 0\} \subset H_0^1(\overline{\Omega})$ be the variation space. The weak form of the problem is: Given $\rho, c_p, u_\infty, f, h, \boldsymbol{\kappa}, \bar{q}, \bar{u}$ as before, find $u \in \mathcal{U}$ such that

$$a(w, u) + a(w, u)_{\Gamma_h} = (w, f) + (w, \bar{q})_{\Gamma_q} + (w, u_\infty)_{\Gamma_h} \quad \forall w \in \mathcal{V}, \tag{9}$$

with bilinear and linear forms

$$a(w, u) = \int_\Omega \left(\nabla w \cdot (\boldsymbol{\kappa}\nabla u) + w\delta(\mathbf{x} - \mathbf{x}_e) c_p \dot{\mathbf{m}}_e \cdot \nabla u \right) d\Omega, \tag{10}$$

$$a(w, u)_{\Gamma_h} = \int_{\Gamma_h} whu \, d\Gamma, \tag{11}$$

$$(w, f) = \int_\Omega wf \, d\Omega, \tag{12}$$

$$(w, \bar{q})_{\Gamma_q} = \int_{\Gamma_q} w\bar{q} \, d\Gamma, \tag{13}$$

$$(w, u_\infty)_{\Gamma_h} = \int_{\Gamma_h} whu_\infty \, d\Gamma. \tag{14}$$

An approximate temperature distribution in the material $u^h(\mathbf{x})$ is obtained by solving Eq. (11) with a finite element discreti-zation of the domain $\overline{\Omega}^h \cong \overline{\Omega}$. Various thermal efficiency objective functions can then be defined, such as the average tem-

perature over the polymeric component, the thermal energy stored, or even the temperature gradients if the stresses produced by the thermal field are of interest. In the examples presented in this paper, we adopt the maximum temperature objective function $\phi_T : \overline{\Omega}^h \to \mathbb{R}$:

$$\phi_T := \max u^h(\mathbf{x}), \quad \forall \mathbf{x} \in \overline{\Omega}^h. \tag{15}$$

4.4. Connectivity constraint

The objective functions introduced above are computed only for networks for which a solution to the flow problem, as outlined in Section 4.2, can be obtained. When the candidate solutions are allowed to change in structure throughout the optimization process, many of the subgraphs $\mathcal{G}'$ of the graph $\mathcal{G}$ that represents the network template become unfeasible. When a solution to the flow problem cannot be computed, the candidate solution is marked as unfeasible. The connectivity constraint is defined as a function $\psi_c : \mathcal{E}'(\mathcal{G}') \to \mathbb{R}$ such that

$$\psi_c := \begin{cases} 1/|\mathcal{E}'(\mathcal{G}')| & \text{if } \mathcal{G}' \text{ is disconnected,} \\ 0 & \text{otherwise.} \end{cases} \tag{16}$$

Because ψ_c is inversely proportional to the number of edges in the candidate solution, the optimization process pushes unfeasible individuals towards a known valid topology, that of the microvascular network template.

5. Validation study

The numeric solution of Eq. (11) is now compared with experimental measurements. Three sets of experimental results are used in this study: (i) the surface temperature of the polymeric component obtained by infrared (IR) imaging of the specimen [1]; (ii) the temperature of the fluid through the two-dye laser induced fluorescence (LIF) technique [27]; and (iii) the mass flow rate in the microchannels via the microscopic particle image velocimetry (μ–PIV) technique [24]. The experimental results used in this validation study for the infrared imaging of the polymer surface and the two-dye LIF were obtained almost simultaneously, whereas mass flow rates were measured at a different time.

The measurement of the temperature field in the polymer is accomplished by obtaining images of the specimen with the aid of an IR camera. The base of the specimen is placed on a copper plate, which in turn lies on a resistive heater that is kept at constant temperature using a feedback controller. Thermally conductive grease is laid along the interface between the copper plate and the fin. The IR camera is utilized to capture the temperature distribution in the surface of the fin that contains the microvascular network. The specimen used in the experiments, which consists of an epoxy polymeric fin with an embedded twelve-channel microvascular network, is illustrated in Fig. 2 and can also be found in Fig. 1d of Kozola et al. [1]. Attachment nozzles are placed at the diverging and converging points of the fanning manifolds to provide the network with inlet and outlet locations. The microchannels have roughly a diameter $D_e = 410$ μm. The height of the specimen is 19.5 mm, and its thickness is 3.5 mm. The portion of the fin where the microchannels are parallel to the heated stage measures 18.4 mm. The mass flow rate in the individual microchannels is measured employing the μ–PIV technique [24]. This method is able to determine the velocity field in a plane spanning the full diameter of a microchannel. The experimental setup for this technique consists mainly of a laser and a camera. In order to obtain the velocity field in a channel, a solution of deionized water mixed with polystyrene microspheres containing a fluorescent red dye is driven through the network. By employing an optical filter, the camera captures the fluorescent light emitted from the particles. By cross-correlating two consecutive images taken by the camera at a specified time interval, the displacement (and therefore the velocity) field can be fully determined, and thereby the mass flow rate through the microchannel.

Finally, the temperature of the fluid is determined by the two-dye LIF technique [27]. The LIF employs a laser and two cameras with appropriate optical filters that are used to capture the emissions from their corresponding dye. One of the dyes is temperature sensitive, whereas the other is temperature insensitive. However, both dyes are sensitive to the incident energy of the laser, hence to remove the effect of variation in incident energy, the ratio of the images taken by the two cameras is used. The setup is calibrated against known temperatures in a water bath that is used to maintain constant temperature, which is additionally measured by a thermocouple.

Fig. 2. Fin specimen used in the validation study consisting of twelve microchannels that fan from inlet and outlet network locations.

Fig. 3(a) summarizes the results of the comparison between numerical predictions and experimental measurements of the temperature field for the specimen illustrated in Fig. 2. The abscissas show the surface temperature along the centerline of the specimen, and the ordinates the normalized coordinate perpendicular to the heated stage. For the first experimental measurement, no flow was driven through the microvascular network. For the other two experimental results, a solution of deionized water with the two dyes used in the LIF technique was pumped through the twelve channels with total mass flow rates $\dot{m}_{S1} = 1$ g/min and $\dot{m}_{S2} = 2.5$ g/min, and the temperature measurements were obtained after achieving steady-state conditions. As expected, the temperature in the specimen drops with increasing values of the mass flow rate.

The *fin equation*, a simplified 1D equation that describes the energy balance that exists between the heat conducted through the fin and the heat convected to the surrounding fluid, can be used to obtain the film coefficient from experimental results. The equation has the form

$$\frac{d^2 u}{dx^2} = \frac{hP}{\kappa A}(u - u_\infty), \tag{17}$$

where P and A are the perimeter and the area, respectively, of the cross section in contact with the copper plate, x is the coordinate normal to this cross section, κ is the conductivity of the polymeric material and h is the heat transfer coefficient (or film coefficient) that characterizes the heat convection between the fin and the surrounding air with temperature u_∞. Boundary conditions include fixed temperature at the base of the fin (in contact with the copper plate) $u|_{x=0} = \bar{u}$, and a convective boundary condition at its free end (i.e., at $x = L = 19.5$ mm) $-\kappa(du/dx)|_{x=L} = h(u(L) - u_\infty)$. With these boundary conditions, the solution to the fin equation is given by

(a)

(b)
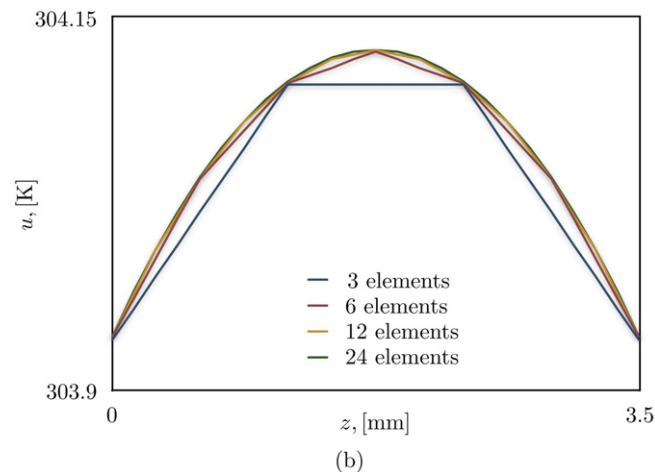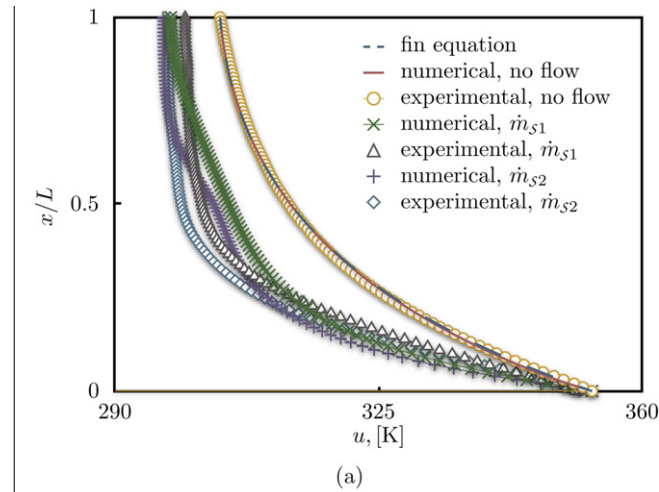
Fig. 3. (a) Temperature profiles obtained at the centerline of the specimen shown in Fig. 2, showing the experimental temperature measurements obtained by infrared imaging, the numerical solutions, and the results of the fin equation. (b) Temperature profile through the thickness obtained numerically at the top of the specimen for meshes with different thickness discretizations.

$$\frac{u(x) - u_\infty}{\bar{u} - u_\infty} = \frac{\cosh\beta(L-x) + \left(\frac{h}{\beta\kappa}\right)\sinh\beta(L-x)}{\cosh\beta L + \left(\frac{h}{\beta\kappa}\right)\sinh\beta L}, \tag{18}$$

$$\beta = \sqrt{\frac{hP}{\kappa A}}.$$

With $\bar{u} = 353.3$ K and an environmental temperature $u_\infty = 296.4$ K, it was found that a heat transfer coefficient $h = 8.1$ W/m² K matches closely the experimental results, as shown by the corresponding dashed curve in Fig. 3(a).

A finite element model of the central portion of the domain that contains the straight microchannels, i.e., $18.4 \times 19.5 \times 3.5$ mm³, is created to obtain the numerical temperature predictions. In the absence of flow, the boundary conditions for the computational model include a temperature $\bar{u} = 353.3$ K, prescribed at the base of the model, and convective boundary conditions along the top and along the two major surfaces. Insulated boundary conditions, i.e., $\bar{q} = 0$, are applied to the remaining surfaces of the computational model. For the convective boundary conditions, the environmental temperature is the same as the one used for the fin equation, and a value $h = 8.7$ W/m² K for the heat transfer coefficient was obtained by matching the measured experimental temperature at the top of the fin. Thus, in the absence of flow, the numerical results match closely those of the fin equation and the experimental results, as illustrated in Fig. 3(a).

A mesh convergence study is carried out by creating four structured meshes of eight-node brick elements over the 3D grids $\left\{40 \times 48 \times 2^i \cdot 3\right\}_{i=0}^{3}$. In other words, the four meshes have 40 elements along the length 18.4 mm, 48 elements along the length 19.5 mm and either 3, 6, 12, or 24 elements through the thickness of 3.5 mm. For the four meshes, measurements of the temperature across the thickness over the top of the specimen are reported in Fig. 3(b). The figure shows that considering six elements is enough to capture the thermal effects through the thickness of the specimen. It also illustrates that the temperature at the extreme sides of the specimen, which are the locations where the temperature measurements can be obtained experimentally by infrared imaging, does not vary much, even when considering only three elements across the thickness.

For the numerical predictions considering the effect of the flow through the microvascular network, the mass flow rate in each microchannel is predicted by taking into account the actual geometry of the specimen. In other words, each microchannel length is measured and its corresponding mass flow rate is obtained from Eq. (2). Also, the temperature of the fluid at inlet locations is prescribed in the computational model with the values reported in Table 1, which were obtained experimentally by the two-dye LIF technique described above. The temperature values of the fluid at other inlet locations were linearly extrapolated from those given in the table. The numerical results that take into account the effect of the flow are also given in Fig. 3(a). It can be seen that the numerical curves follow the same trend as the experimental ones, which means that the temperature reduces as the mass flow rate increases. Also, both numerical and experimental results share the same order of magnitude, but there are some discrepancies between them. The first source of discrepancy is associated with the experimental error related to the temperature measurements at inlet locations and with the interpolation/extrapolation of the temperature values given in Table 1 for the other eight microchannels. Another source of discrepancy is due to the departure of the predicted flow distribution across the twelve microchannels used for the numerical simulations from the actual flow field in the experiments. Indeed, as shown in Fig. 4(a), a substantial variability is observed experimentally (using the μ−PIV technique), with some channels (especially the center ones) carrying more of the flow than others. Taking that variability into account in the numerical predictions leads to the results shown in Fig. 4(b). As apparent there, the differences observed in the temperature profile due to the variability in mass flow rate are negligible for the case $\dot{m}_{s1} = 1$ g/min. Therefore, the remaining discrepancy is probably associated with errors in the inflow temperature, emphasizing the need for the simultaneous measurement of the fin surface temperature and the inflow temperature of the cooling fluid in every microchannel.

6. Network optimization results

This section presents the results obtained by applying the optimization framework for the design of 3D microvascular polymeric components to two different applications. The first application consists of the design of a periodic microvascular

Table 1
Fluid temperature values obtained by the two-dye LIF technique, given in Kelvin, measured at the start of the straight portion of four microchannels for the specimen illustrated in Fig. 2. Channel 2 is the closest channel to the heated stage.

Channel	Mass flow rate $\dot{m}$, 1	[g/min] 2.5
2	312.4	311.9
4	309.5	305.8
7	305.2	305.1
8	303.2	297.0
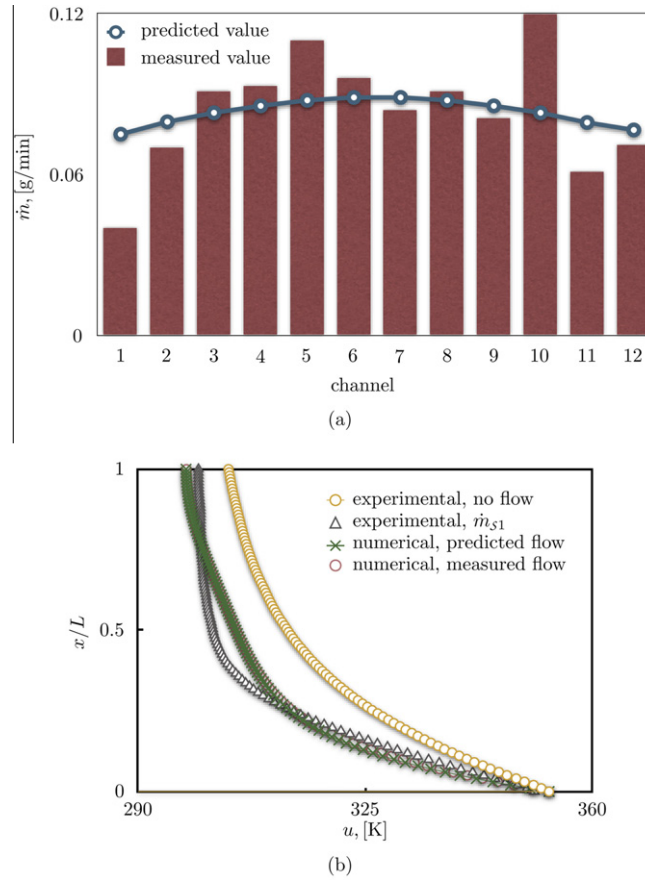
Fig. 4. (a) Predicted and measured mass flow rate values for each of the twelve channels for a total mass flow rate $\dot{m}_{S1} = 1$ g/min. (b) Temperature profiles at the centerline of the fin specimen showing numerical and experimental results for the same mass inflow rate, and the experimental curve in the absence of flow for reference.

cell that is part of a larger polymeric component, e.g., a thin wall structure used for high temperature applications. The second application is motivated by the 2D optimization problem involving two localized heat sources discussed previously in [2].

6.1. Periodic microvascular cell

Consider a cubic domain $\Omega = a^3$ with $a = 10$ mm, as displayed in Fig. 5. The figure shows a part of the microvascular network template $\mathcal{G}$, which contains 1946 microchannels. With a diameter set $\mathcal{D}[\mu m] = \{0, 100\}$ used in the optimization process, there are 2^{1946} possible network configurations. As mentioned previously, even though many of these topologies are not feasible because they result in disconnected networks for the flow problem, the number of feasible structures is extremely large. The network template consists of channels with length $L_e = 1$ mm aligned over an n^3 grid (with $n = 8$), with a total of $3n(n+1)^2$ microchannels, plus two more that link inflow and outflow with the rest of the network. Thus, the network template has roughly a 1 mm cover from each of the six surface domain boundaries. A single inflow and a single outflow are located at the bottom surface and are displayed using arrows in the figure. Flow boundary conditions comprise a prescribed mass inflow rate $\dot{m}_S = 1$ g/min at the inlet and zero pressure at the outlet. The fluid used as coolant is water, with kinematic viscosity $v = 1.05 \times 10^{-6}$ m^2/s and specific heat $c_p = 4185.5$ J/kg K. Results are reported only for constant inflow, so that the mass inflow rate does not change in all individual evaluations (see reference [2] for further details). For the heat boundary value problem, a thermal conductivity value of $\kappa = 0.3$ W/mK is used for the polymer. A uniform heat flux $\bar{q} = 3$ kW/m^2 is applied to the top surface and the bottom surface has a prescribed temperature $\bar{u} = 273.15$ K, which is also the temperature of the incoming fluid. Thus, in the absence of flow the temperature field has a linear variation in the z coordinate, with a maximum temperature $u_{max} = 373$ K over the top surface. The remaining surfaces have a periodic boundary condition, thus defining a unit microvascular cell in the x and y directions, as displayed by the coordinate axes in the figure. The cubic domain is discretized with a structured finite element mesh, consisting of $20 \times 20 \times 20 = 8000$ eight-noded brick elements and
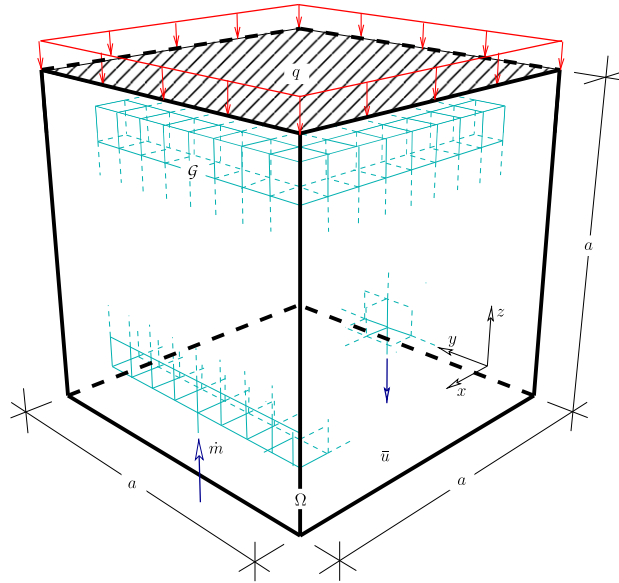
Fig. 5. Schematic of the periodic microvascular cell problem with cubic domain $\Omega = a^3$ and part of the microvascular network template $\mathcal{G}$. A single inflow and a single outflow are displayed in the figure with arrows. A uniform heat flux $\bar{q}$ is applied at the top surface, and a temperature $\bar{u}$ is prescribed at the bottom surface. The remaining surfaces have periodic boundary conditions, thus defining a unit cell periodic in the x and y directions.

a total of 9261 nodes. Note that a matching finite element mesh is used, thus the microchannels of the network template lie along the edges of finite elements in the mesh. By analyzing the grids used for discretizing the domain and for outlining the microvascular network template, it can be inferred that each microchannel is surrounded by eight brick elements.

The optimization problem is then stated as:

$$\text{minimize } \Phi = \left\{ \phi_v, \phi_f, \phi_T \right\},$$
$$\text{such that } \psi_c = 0.$$

The problem is then optimized with a population size $|\mathcal{P}| = 1000$. The Pareto-optimal front for this problem is displayed in Fig. 6 at generation $t = 10000$. Selected candidate solutions, labeled in the figure and marked with $\diamond, \bigcirc$, and $\square$ symbols, are presented in Fig. 7. The front is projected into three orthogonal planes to ease its visualization. The projections show a well-defined surface, with some individuals isolated from the main population, e.g., those marked with $\diamond, \bigcirc$ symbols. In Fig. 7, the upper row shows the temperature field, whereas the lower row shows the corresponding network and flow field. In the lower figures, the arrows that represent the flow are color-coded and scaled according to their flow magnitude.

The candidate solution that minimizes the value of ϕ_v, marked with a $\diamond$ symbol in Fig. 6, is presented in Figs. 7(a) and (d). This is the most optimal solution for this objective function, as the inlet and the outlet are connected using the least number of microchannels, as revealed by Fig. 7(d). On the other hand, this solution is the worst for minimizing the maximum temperature objective function ϕ_T, reducing it by only 1 K from the configuration without flow. Note that this individual is isolated in the front from the main population. The individual that maximizes the flow efficiency is shown in Figs. 7(e) and is marked with a $\bigcirc$ symbol in the Pareto-optimal front of Fig. 6. The network is very dense, so that its topology resembles that of the microvascular network template. After dividing the flow into four paths close to the inlet, the magnitude of the flow is reduced and rapidly becomes negligible close to the upper surface. The maximum temperature for this solution is reduced by approximately 54 K. Finally, the candidate solution that minimizes ϕ_T, corresponding to Figs. 7(c) and (f), is marked with a $\square$ symbol in the Pareto-optimal front of Fig. 6. This individual reduces the maximum temperature by approximately 84 K. Fig. 7(f) shows how the fluid is pushed from the inlet to the upper surface where the uniform heat flux is applied. Along the upper surface, the flow seems to be uniformly distributed. Then the flow is collected in the other side of the domain and taken to the outlet. Note the absence of microchannels in the interior of the domain, demonstrating that no network is required in this region to minimize the temperature. Referring back to Fig. 6, it can be seen that this individual has a low value of the flow efficiency objective function ϕ_f. Dividing the flow in the upper surface has the effect of reducing the amount of energy needed to drive the flow, with the penalty of increasing the void volume fraction. Thus, this individual has also a high value of ϕ_v. It is worth mentioning that the candidate solutions that minimize ϕ_v and ϕ_f, shown in Figs. 7(d) and (e), respectively, have a similar value of the flow efficiency objective function. Thus, for the dense network the division of the flow in several paths compensates the increase in length, thus maintaining a low value for the pressure drop between inlet and outlet locations.
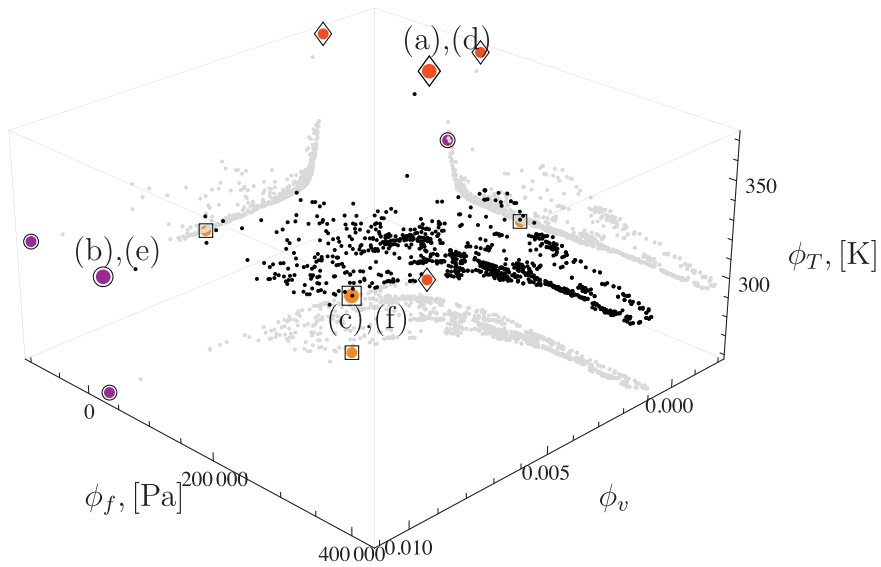
Fig. 6. Pareto-optimal surface at generation $t = 10000$ for the periodic cell example. Individuals selected for visualization are displayed in Fig. 7 and are labeled in the front and marked with $\diamond, \circ, \square$ symbols.
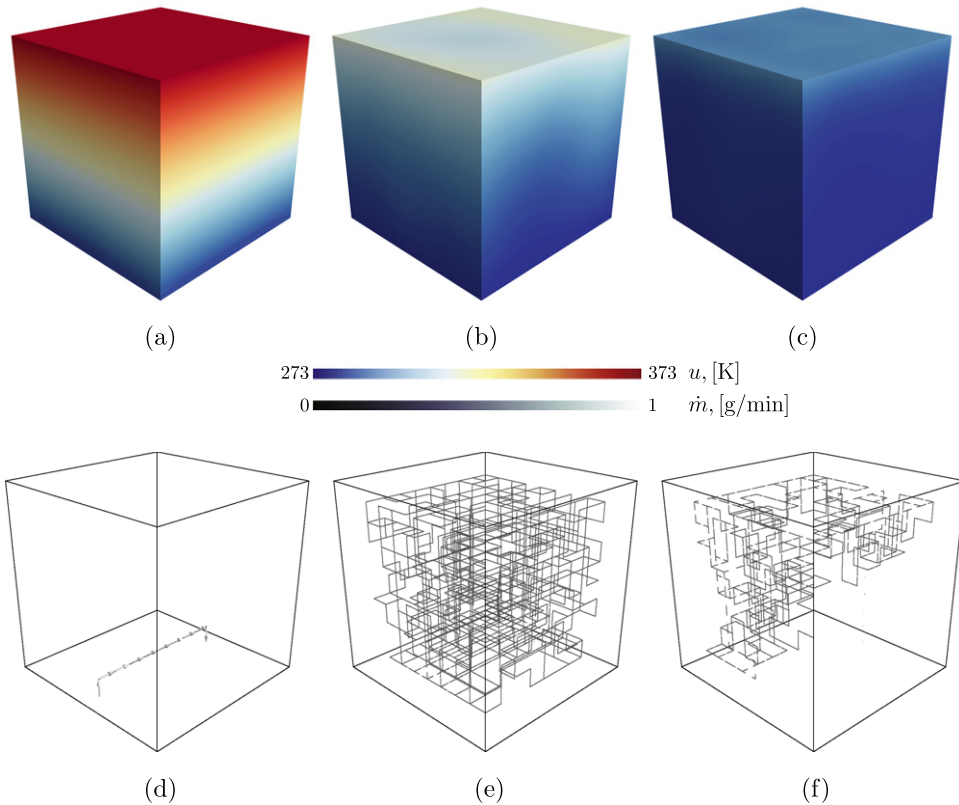
Fig. 7. Selected candidate solutions at generation $t = 10000$, marked in the Pareto-optimal front of Fig. 6 with $\diamond, \circ$, and $\square$ symbols. The upper row shows the temperature field, whereas the figures in the lower row show the corresponding flow field with their corresponding network. Figures (a) and (d) correspond to the individual that minimizes ϕ_v, figures (b) and (e) to the individual that minimizes ϕ_f and figures (c) and (f) to the one that minimizes ϕ_T. Arrows are size-coded according to flow magnitude.
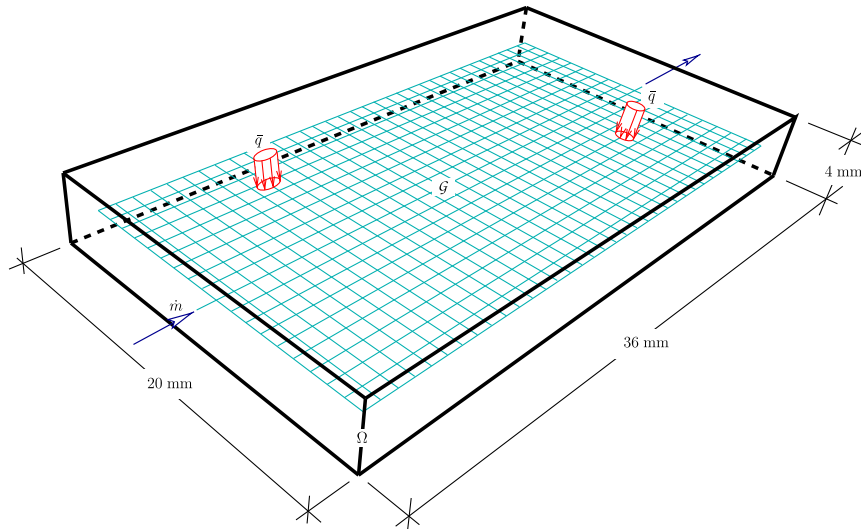
Fig. 8. Schematic of the mathematical model for the localized heating example, showing the domain Ω and the microvascular network template $\mathcal{G}$ used in the optimization process. Arrows show the location of the inflow and outflow for the flow problem. For the heat boundary value problem, a localized heat flux $\bar{q}$ is applied in two locations over the top surface.

6.2. Microvascular fin with localized heating

Consider the domain $\Omega = (36 \times 20 \times 4)$ mm^3, confined by the rectangular cuboid shown in Fig. 8. For this problem, the microvascular network template is aligned along a 2D $m \times n$ grid over the specimen's plane of symmetry that is parallel to the main surfaces. Thus, the network has $m + n + 2mn$ channels, plus a couple used to connect with the flow boundary locations. With $m = 34$ and $n = 18$, there are a total of 1278 microchannels. As in the previous problem, all microchannels have a length $L_e = 1$ mm, and the polymeric component has a cover of roughly 1 mm in each side over the plane of the network, and a cover of 2 mm in the direction perpendicular to its plane. A diameter set $\mathcal{D}[\mu m] = \{0, 100\}$ is used throughout the optimization process, resulting in 2^{1278} network configurations. For the flow boundary value problem, a single prescribed mass inflow rate of water $\dot{m}_S = 1$ g/min and zero pressure are considered as boundary conditions, and their locations are displayed in the figure with arrows. The coolant properties are the same as those given in the previous example. Regarding the solution of the thermal boundary value problem, the rectangular cuboid is discretized using a structured mesh of eight-node brick elements, with a total of $72 \times 40 \times 8 = 23040$ finite elements and 26937 nodes. Thus, this example contains a much larger number of elements compared to the periodic microvascular cell problem studied in the preceding example. A heat flux $\bar{q}$ is applied locally as displayed in the figure to the free surface of eight finite elements, i.e., to four elements per localized heat source. Convective boundary conditions, with ambient temperature $u_\infty = 293.15$ K and heat transfer coefficient $h = 1.78$ W/m^{2}K, are prescribed along every surface of the domain that does not contain the applied heat fluxes. The surface that contains the applied heat flux is considered insulated in the portions that do not contain the heat flux. The 3D temperature field given in Fig. 9 is our reference solution in the absence of flow for the optimization process. The value of the prescribed inlet fluid temperature is $\bar{u} = 283.15$ K.

283 ▮▮▮▮▮▮▮▮▮▮▮▮▮▮▮ 369 $u, [\text{K}]$
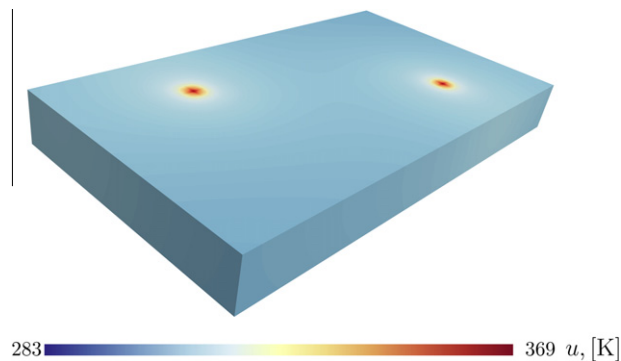
Fig. 9. Temperature distribution in the absence of flow for the thermal boundary value problem shown in Fig. 8, taken as the reference temperature field for the full 3D GA optimization.
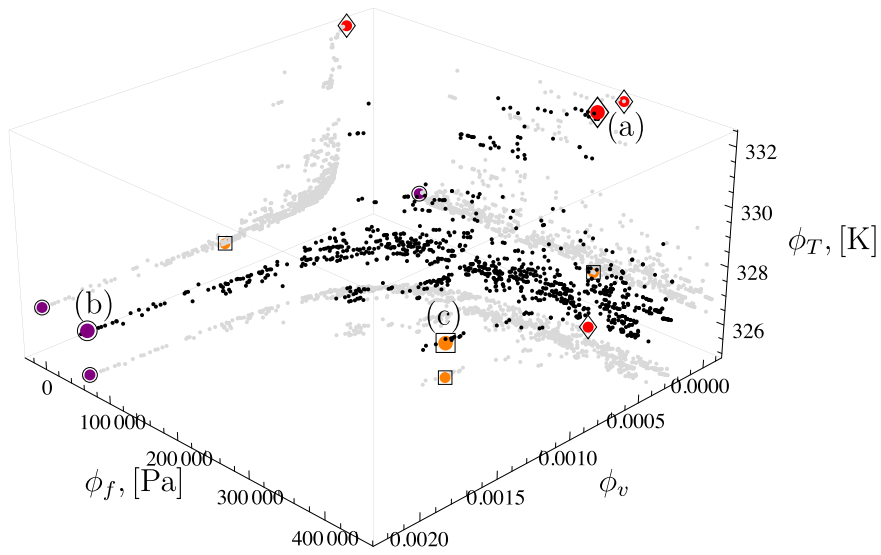
Fig. 10. Pareto-optimal surface at generation $t = 5000$ for the localized heating example. The optimization is carried out using the 3D finite element model illustrated in Fig. 9. Selected candidate solutions are displayed in Fig. 11 and are labeled in the front and marked with $\diamond, \circ, \square$ symbols.
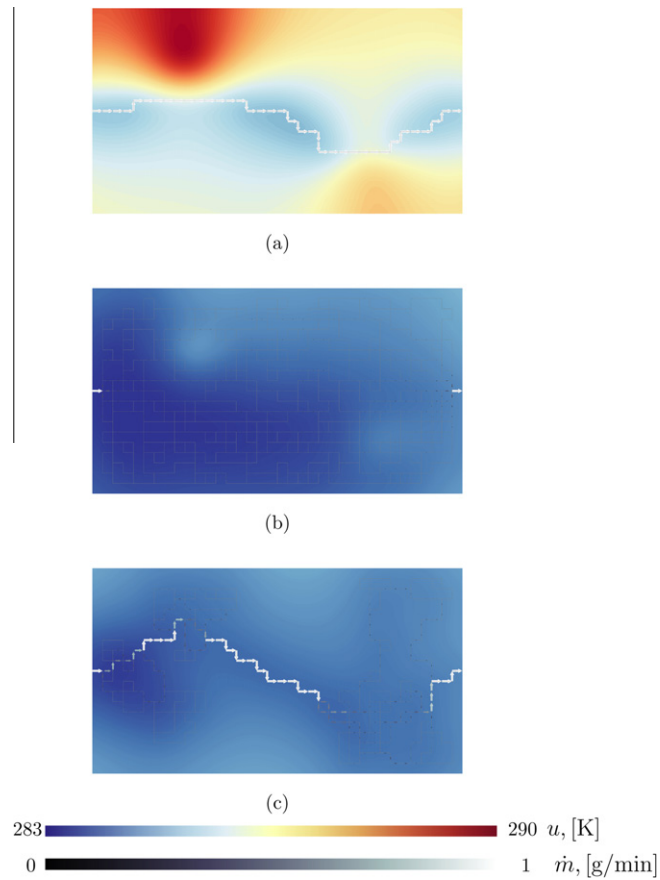
Fig. 11. Selected individuals for the localized heating example obtained with the conventional GA scheme after 5000 generations with a population size $|\mathcal{P}| = 1000$. The figures show the temperature field at the surface opposite to where the localized heat sources are applied, and their corresponding networks and flow fields projected on this surface. The temperature range is defined as the minimum and maximum temperature values in the figures. The candidate solutions shown in Figures (a), (b), and (c), minimize objective functions ϕ_v, ϕ_f, and ϕ_T, respectively.

Two approaches are considered to optimize the microvascular network: The first one considers a full 3D optimization, i.e., the thermal boundary value problem is solved using the finite element model used to obtain the temperature field displayed in Fig. 9. The second one uses the aid of a 2D optimization by exploiting the two-dimensional nature of the microvascular network template. In other words, a 2D GA optimization can be carried out, and the resulting population from the evolution process can then be used as the starting population for a 3D optimization. Thus, the starting population of the 3D optimization is not random anymore, so particular features about optimal solutions are incorporated into the optimization. This type of optimization belongs to the aforementioned category of knowledge-based GAs.

For the full 3D optimization, a population size $|\mathcal{P}| = 1000$ is used, and the NSGA-II results at generation $t = 5000$ are displayed in Fig. 10. As before, the front is projected into three orthogonal planes to ease the visualization. Because the evaluation of the population at a particular generation is proportional to the evaluation time of the individual objective functions, and because of the large finite element mesh used to solve this problem in 3D, the total computational time is dramatically increased with respect to the solution of the previous problem. Three individuals on the front, marked with $\diamond, \bigcirc$, and $\square$ symbols, are displayed in Fig. 11. The selected individuals show the temperature field over the boundary surface opposite to where the localized heating is applied, together with their corresponding network and flow field. Arrows in the figure are again scaled according to the magnitude of the flow. The individual shown in Fig. 11(a) minimizes the value of ϕ_v in this generation. Clearly, this solution approaches the optimal configuration for this objective function, which connects the inflow and outflow with a straight path. The candidate solution presented in Fig. 11(b) maximizes the flow efficiency, and it has a very dense network structure, resembling as before that of the microvascular network template. Finally, the individual in Fig. 11(c) minimizes the maximum temperature objective function ϕ_T. It can be noted that the flow is spread close to the hot spots.

For the second set of results, the thermal boundary value problem is solved using a 2D structured finite element discretization of the main surface, with 5760 three-node elements and 2993 nodes. The applied heat flux is scaled in order to match the maximum temperature field in the heated substrate. The 2D evolution uses a population size $|\mathcal{P}| = 3200$ and the selected individuals at generation $t = 10000$ that minimize objective functions ϕ_v, ϕ_f, and ϕ_T are displayed in Fig. 12. It is worth mentioning that considerable computational time savings are obtained from using a 2D solution for the thermal

(a)

(b)

(c)
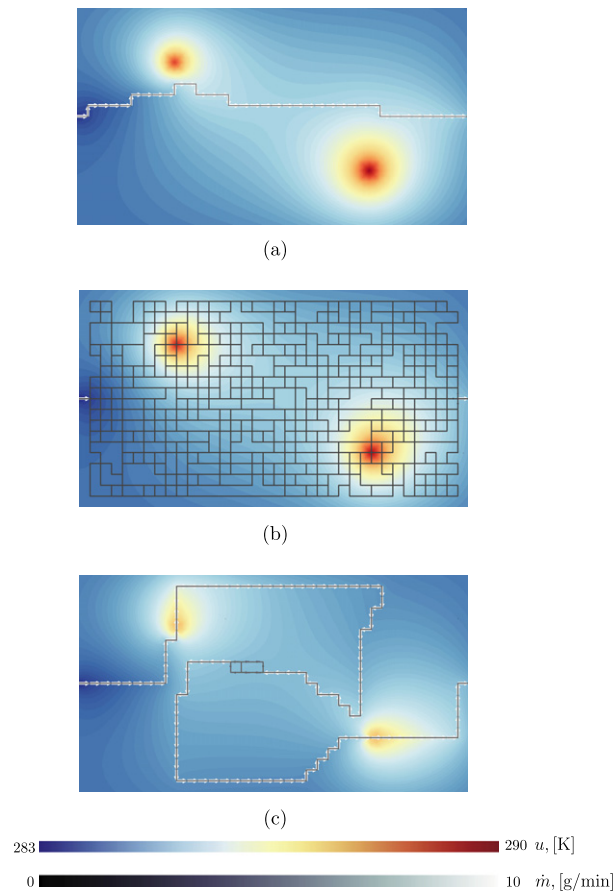
Fig. 12. Figures (a), (b), and (c) show the selected individuals at generation $t = 10000$ of the 2D optimization, minimizing ϕ_v, ϕ_f, and ϕ_T, respectively.
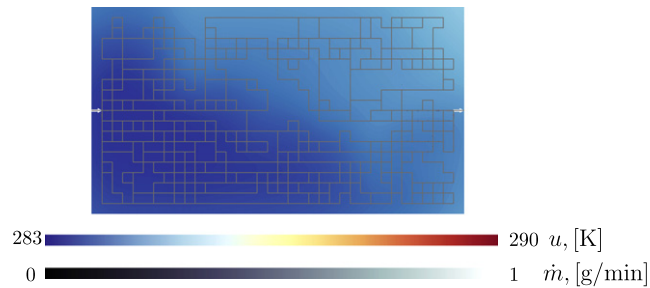
Fig. 13. Candidate solution that minimizes the maximum temperature objective function ϕ_T for the knowledge-based GA optimization that started with the evolved population at generation $t = 9900$ of the 2D optimization. The figure shows the temperature field in the surface located away from the application of the heat sources.

boundary value problem, as the latter optimization resulted roughly in 3% of the total time spent by the full 3D optimization. Note also that for the 2D optimization, the number of generations were doubled and that a much larger population size was used. The individuals that minimize ϕ_v and ϕ_f objective functions, shown in Figs. 12(a) and (b), are similar to those shown in Figs. 11(a) and (b). However, the candidate shown in Fig. 12(c) is remarkably different. As in reference [2], the flow is collected into a single path of microchannels that pass through the two hot regions of the domain. The maximum temperature in the 3D computational model considering the network of Fig. 12(c) is $u_{max} = 327.9$ K. On the other hand, the individual shown in Fig. 11(c) seems to distribute the flow close to the hot regions, so it would seem that this solution is not the most effective in cooling down the polymeric component. Nevertheless, the maximum temperature in the polymeric component is $u_{max} = 326.2$ K, which is 1.7 K below the earlier temperature value.

The 2D population at generation $t = 9900$ is now taken as the starting point for the 3D optimization, and the algorithm is evolved only 100 generations. The candidate that minimizes ϕ_T at generation $t = 10000$ for this knowledge-based evolution is illustrated in Fig. 13. This solution has a maximum temperature that is only 0.162 K higher than the individual in Fig. 11(c). Thus the network displayed in Fig. 12(c) is not the most optimal one at minimizing the maximum temperature objective function ϕ_T. Because the heat sources are applied at a plane parallel to that of the microvascular network template, and because of the diffusion of the heat that spreads the hot regions at the plane of the network, the optimal solutions from 2D and 3D cases are remarkably different. However, it is worth noting that a Pareto-optimal front can be obtained faster with the aid of a 2D optimization in these cases.

7. Conclusions

This work has extended the framework presented by the authors in [2] to the optimization of three-dimensional microvascular flow networks embedded in polymeric materials. The approach has combined the NSGA-II optimization scheme with a finite element solver used to predict the impact of the embedded network on the thermal field in the microvascular component. A validation study aimed at closing the gap between experimental measurements and computational predictions. It was shown that the mathematical model used to represent the cooling at microchannels was able to predict cooling effects with the same order of magnitude as those obtained experimentally. However, discrepancies were observed, mainly because of the lack of data for the fluid temperature at inlet locations. Other objective functions have included the flow efficiency and void volume fraction of the network of microchannels.

A drawback of the proposed method is undoubtedly its computational cost, as the objective functions associated with the population members need to be evaluated at every generation. However, the computation of these objective functions is embarrassingly parallel, and the implementation of the framework on distributed memory architectures results in almost ideal speed-up. The results showed that the trade-offs among competing objectives were accurately captured in a Pareto-optimal front, from which the analyst can readily determine the candidate solution that suits a particular problem. However, while the optimum solutions along the Pareto front were readily obtained, these candidate solutions alternated locations over the front in subsequent generations. Furthermore, because of the crowding distance parameter [16], the algorithm could exchange optimal solutions in tightly crowded areas for non-optimal solutions. To circumvent this drawback, the NSGA-II could be swapped by other multi-objective evolutionary strategy [28].

Despite these issues, the NSGA-II optimization scheme adopted in this study has proven to be a viable alternative for the multi-physics design of these materials, by considering a set of objective functions associated with different physical phenomena. No further complexity is introduced to the framework by adding objective functions or constraints, and the methodology presented can accommodate an arbitrary number of them.

Two applications have been considered in this work. The first one involved a periodic microvascular cell that is part of a larger polymeric component subjected to a uniform heat flux. In the second application, which focused on the design of a microvascular fin with a planar embedded network, it was shown that the results of a 2D optimization can be used to speed up the more complex and computationally intensive 3D optimization. This methodology, referred to as knowledge-based GA,

incorporated knowledge about optimal topologies into the starting population chosen among the evolved population of a 2D optimization. This application showed that, while not fully optimum, the results of the knowledge-based GA are close to those provided by the conventional GA optimization, for which the population was chosen randomly.

Acknowledgments

References

[1] B.D. Kozola, L.A. Shipton, V.K. Natrajan, K.T. Christensen, S.R. White, Characterization of active cooling and flow distribution in microvascular polymers, Journal of Intelligent Material Systems and Structures (2010), http://dx.doi.org/10.1177/1045389X10379662.
[2] A.M. Aragón, K.J. Smith, P.H. Geubelle, S.R. White, Multi-physics design of microvascular materials for active cooling applications, Journal of Computational Physics 230 (13) (2011) 5178–5198, http://dx.doi.org/10.1016/j.jcp. 2011.03.01.
[3] K.S. Toohey, N.R. Sottos, J.A. Lewis, J.S. Moore, S.R. White, Self-healing materials with microvascular networks, Nature Materials 6 (8) (2007) 581–585, http://dx.doi.org/10.1038/nmat1934.
[4] C. Hansen, W. Wu, K. Toohey, N. Sottos, S. White, J. Lewis, Self-healing materials with interpenetrating microvascular networks, Advanced Materials 21 (41) (2009) 4143–4147, http://dx.doi.org/10.1002/adma.200900588.
[5] D. Therriault, S.R. White, J.A. Lewis, Chaotic mixing in three-dimensional microvascular networks fabricated by direct-write assembly, Nature Materials 2 (4) (2003) 265–271, http://dx.doi.org/10.1038/nmat863.
[6] W. Wu, A. DeConinck, J.A. Lewis, Omnidirectional printing of 3d microvascular networks, Advanced Materials 23 (24) (2011) H178–H183, http://dx.doi.org/10.1002/adma.201004625.
[7] A.P. Esser-Kahn, P.R. Thakre, H. Dong, J.F. Patrick, V.K. Vlasko-Vlasov, N.R. Sottos, J.S. Moore, S.R. White, Three-dimensional microvascular fiber-reinforced composites, Advanced Materials (2011) n/a–n/a, http://dx.doi.org/10.1002/adma.201100933.
[8] A. Bejan, S. Lorente, Constructal theory of generation of configuration in nature and engineering, Journal of Applied Physics 100 (4) (2006) 041301, http://dx.doi.org/10.1063/1.2221896.
[9] A. Bejan, S. Lorente, The constructal law and the evolution of design in nature, Physics of Life Reviews 8 (3) (2011) 209–240, http://dx.doi.org/10.1016/j.plrev.2011.05.010.
[10] A. Bejan, S. Lorente, K.-M. Wang, Networks of channels for self-healing composite materials, Journal of Applied Physics 100 (3) (2006) 033528, http://dx.doi.org/10.1063/1.2218768.
[11] H. Zhang, S. Lorente, A. Bejan, Vascularization with trees that alternate with upside-down trees, Journal of Applied Physics 101 (9) (2007) 094904, http://dx.doi.org/10.1063/1.2723186.
[12] S. Kim, S. Lorente, A. Bejan, Vascularized materials: tree-shaped flow architectures matched canopy to canopy, Journal of Applied Physics 100 (6) (2006) 063525, http://dx.doi.org/10.1063/1.2349479.
[13] A. Klarbring, J. Petersson, B. Torstenfelt, M. Karlsson, Topology optimization of flow networks, Computer Methods in Applied Mechanics and Engineering 192 (35, 36) (2003) 3909–3932, http://dx.doi.org/10.1016/S0045-7825(03). 00393-1.
[14] D.E. Goldberg, Genetic Algorithms in Search, Optimization, and Machine Learning, Addison-Wesley Publishing Company, Massachusetts, 1989.
[15] D.E. Goldberg, The Design of Innovation: Lessons from and for Competent Genetic Algorithms, Kluwer Academic Publishers, Massachusetts, 2002.
[16] K. Deb, Multi-Objective Optimization Using Evolutionary Algorithms, 1st Edition., John Wiley & Sons Inc., 2001.
[17] A.M. Aragón, J.K. Wayer, P.H. Geubelle, D.E. Goldberg, S.R. White, Design of microvascular flow networks using multi-objective genetic algorithms, Computer Methods in Applied Mechanics and Engineering 197 (49–50) (2008) 4399–4410, http://dx.doi.org/10.1016/j.cma.2008.05.025.
[18] A.M. Aragón, C.A. Duarte, P.H. Geubelle, Generalized finite element enrichment functions for discontinuous gradient fields, International Journal for Numerical Methods in Engineering 82 (2) (2010) 242–268, http://dx.doi.org/10.1002/nme.2772.
[19] A. Bejan, S. Lorente, Design with Constructal Theory, John Wiley & Sons, Inc, 2008.
[20] T. Borrvall, A. Klarbring, J. Petersson, B. Torstenfelt, M. Karlsson, Topology optimization in fluid mechanics, in: Proceedings of the 5th WCCM V, World Congress on Computational Mechanics, Vienna, vol. 7, 2002, p. 12.
[21] T. Borrvall, J. Petersson, Topology optimization of fluids in stokes flow, International Journal for Numerical Methods in Fluids 41 (1) (2003) 77–107, http://dx.doi.org/10.1002/fld.426.
[22] V. Pareto, Manuale di Economia Politica, Piccola Biblioteca Scientifica, Milan, 1906, translated into English by Ann S. Schwier (1971), Manual of Political Economy, MacMillan, London.
[23] K. Deb, A. Pratap, S. Agarwal, T. Meyarivan, A fast and elitist multiobjective genetic algorithm: NSGA-II, IEEE Transactions on Evolutionary Computation 6 (2) (2002) 182–197, http://dx.doi.org/10.1109/4235.996017.
[24] V. Natrajan, K. Christensen, Microscopic particle image velocimetry measurements of transition to turbulence in microscale capillaries, Experiments in Fluids 43 (1) (2007) 1–16, http://dx.doi.org/10.1007/s00348-007-0301-7.
[25] C.A. Brebbia, A.J. Ferrante, Computational Hydraulics, Butterworth-Heinemann Ltd, London, 1983.
[26] W.M. Kays, M.E. Crawford, B. Weigand, Convective Heat and Mass Transfer, 4th ed., McGraw-Hill, 2004.
[27] V.K. Natrajan, K.T. Christensen, Two-color laser-induced fluorescent thermometry for microfluidic systems, Measurement Science and Technology 20 (1) (2009) 015401, http://dx.doi.org/10.1088/0957-0233/20/1/015401.
[28] S. Kukkonen, J. Lampinen, GDE3: the third evolution step of generalized differential evolution, in: The 2005 IEEE Congress on Evolutionary Computation, Vol. 1, Edinburgh, Scotland, 2005, pp. 443–450, http://dx.doi.org/10.1109/CEC.2005.1554717.